

## Groyne-Induced Effects on Channel-Shoal Exchange and Saltwater Intrusion in Estuarine Environments

Zhou, Zaiyang; Ge, Jianzhong; Van Maren, D. S.; Kuai, Yu; Ding, Pingxing; Wang, Zheng Bing

**DOI**

[10.1061/JHEND8.HYENG-13500](https://doi.org/10.1061/JHEND8.HYENG-13500)

**Publication date**

2023

**Document Version**

Final published version

**Published in**

Journal of Hydraulic Engineering

**Citation (APA)**

Zhou, Z., Ge, J., Van Maren, D. S., Kuai, Y., Ding, P., & Wang, Z. B. (2023). Groyne-Induced Effects on Channel-Shoal Exchange and Saltwater Intrusion in Estuarine Environments. *Journal of Hydraulic Engineering*, 150(1), Article 04023056. <https://doi.org/10.1061/JHEND8.HYENG-13500>

**Important note**

To cite this publication, please use the final published version (if applicable). Please check the document version above.

**Copyright**

Other than for strictly personal use, it is not permitted to download, forward or distribute the text or part of it, without the consent of the author(s) and/or copyright holder(s), unless the work is under an open content license such as Creative Commons.

**Takedown policy**

Please contact us and provide details if you believe this document breaches copyrights. We will remove access to the work immediately and investigate your claim.

***Green Open Access added to TU Delft Institutional Repository***

***'You share, we take care!' - Taverne project***

**<https://www.openaccess.nl/en/you-share-we-take-care>**

Otherwise as indicated in the copyright section: the publisher is the copyright holder of this work and the author uses the Dutch legislation to make this work public.



# Groyne-Induced Effects on Channel-Shoal Exchange and Saltwater Intrusion in Estuarine Environments

Zaiyang Zhou, Ph.D.<sup>1</sup>; Jianzhong Ge, Ph.D.<sup>2</sup>; D. S. van Maren<sup>3</sup>; Yu Kuai<sup>4</sup>; Pingxing Ding<sup>5</sup>; and Zheng Bing Wang<sup>6</sup>

**Abstract:** Existing knowledge about groyne-induced effects is primarily based on riverine or coastal environments where salinity gradients are absent or limited. However, in estuaries, salinity gradients drive physical processes such as longitudinal and lateral residual flows. The effect of groynes is much more complex because they can modulate channel hydrodynamics and directly affect lateral salinity gradients. In this study, an idealized model is applied to investigate the effects of groyne layouts in estuarine environments, including effects on (1) channel hydrodynamics, (2) lateral water exchange, (3) Coriolis effects, and (4) saltwater intrusion. Model results show that the aspect ratio (the width of groyne fields to the length of groynes) of groyne fields plays an important role. Groynes also induce asymmetry of lateral flows, for example, increasing near-bottom shoal-to-channel flows during low water slack. The aspect ratio has opposite effects on horizontal and vertical components of water exchange. A large aspect ratio strengthens horizontal exchange and weakens density-driven currents. For a large-scale groyne field (several kilometers), Coriolis effects introduce a substantial difference in exchange mechanisms along the north and south banks. A medium range of aspect ratio (2.0–3.0) leads to the strongest saltwater intrusion during both neap and spring tides. **DOI: 10.1061/JHEND8.HYENG-13500.** © 2023 American Society of Civil Engineers.

**Practical Applications:** Dikes and groynes are common engineering structures in waterways designed to increase along-channel flow velocities and prevent sediment deposition, thereby maintaining navigability. However, especially in estuarine environments, cross-channel flow velocities resulting from these structures may generate sediment transport toward the channel, in contrast to their original intention. Another important impact of these structures is on saltwater intrusion, which is crucial to freshwater resource management. Therefore, this research investigates the groyne-induced effects on cross-channel flows and the saltwater intrusion problem by comparing different layouts of groynes and their consequences. Two important findings may benefit practical applications. First, the interaction between saltwater and freshwater in estuaries enhances cross-channel flows during certain periods, thereby influencing sediment transport. Second, the maximal saltwater intrusion occurs for intermediate width-to-length ratios of the groynes, with lower saltwater intrusion for either very small or very wide groyne fields.

<sup>1</sup>Postdoctoral Researcher, State Key Laboratory of Estuarine and Coastal Research, East China Normal Univ., Shanghai 200241, China. Email: zyzhou@sklec.ecnu.edu.cn

<sup>2</sup>Professor, State Key Laboratory of Estuarine and Coastal Research, East China Normal Univ., Shanghai 200241, China; Research Scientist, Institute of Eco-Chongming, Shanghai 202162, China (corresponding author). Email: jzge@sklec.ecnu.edu.cn

<sup>3</sup>Professor, State Key Laboratory of Estuarine and Coastal Research, East China Normal Univ., Shanghai 200241, China; Senior Researcher, Faculty of Civil Engineering and Geosciences, Delft Univ. of Technology, Delft 2628 CN, Netherlands; Specialist, Dept. of Marine and Coastal Systems, Deltares, Delft 2600 MH, Netherlands. Email: bas.vanmaren@deltares.nl

<sup>4</sup>Ph.D. Candidate, Faculty of Civil Engineering and Geosciences, Delft Univ. of Technology, Delft 2628 CN, Netherlands. ORCID: <https://orcid.org/0000-0002-0925-4731>. Email: y.kuai@tudelft.nl

<sup>5</sup>Professor, State Key Laboratory of Estuarine and Coastal Research, East China Normal Univ., Shanghai 200241, China. Email: pxding@sklec.ecnu.edu.cn

<sup>6</sup>Professor, Faculty of Civil Engineering and Geosciences, Delft Univ. of Technology, Delft 2628 CN, Netherlands; Senior Expert, Dept. of Marine and Coastal Systems, Deltares, Delft 2600 MH, Netherlands. ORCID: <https://orcid.org/0000-0002-8787-4530>. Email: zheng.wang@deltares.nl

Note. This manuscript was submitted on September 10, 2022; approved on August 18, 2023; published online on October 20, 2023. Discussion period open until March 20, 2024; separate discussions must be submitted for individual papers. This paper is part of the *Journal of Hydraulic Engineering*, © ASCE, ISSN 0733-9429.

## Introduction

Dikes and groynes have been widely used around the world to regulate and modify hydrodynamics, sediment dynamics, and morphodynamics in rivers, estuaries, and coasts (Yossef and de Vriend 2011). They are hard coastal protection structures that aim to promote navigation and to protect the shoreline from coastal erosion. In riverine and estuarine environments, dikes are usually long structures parallel to flow direction, whereas groynes are perpendicular to flow direction and have a relative shorter length compared with dikes.

Groynes are mostly used in rivers and coastal zones. In river channels, they are mainly used to narrow the channel and increase the flow velocity, thereby increasing the sediment transport capacity, and consequently improve the channel navigability. In coastal zones, they are usually constructed perpendicular to shorelines, functioning as a protection for coasts and beaches from being eroded by alongshore wave-driven currents. Up to now, the effects of groynes were primarily investigated in the context of (1) two-dimensional (2D) hydrodynamic exchange mechanisms, e.g., horizontal eddy (Sukhodolov et al. 2002), turbulence and shear (Uijtewaal 2005), water exchange (Uijtewaal et al. 2001), (2) sediment related issues, e.g., sediment exchange (McCoy et al. 2007; Yossef and de Vriend 2011), sedimentation and morphodynamics (Glas et al. 2018; Sukhodolov et al. 2002), and (3) three-dimensional (3D) flow patterns within the groyne fields (Biron et al. 2005; Ouillon and Dartus 1997) influencing the residence

time within the groyne field (Tritthart et al. 2009). But although groynes are more and more constructed in estuaries, one aspect of groynes that has not been systematically investigated is the role of salinity-driven exchange flows.

Groynes are also applied in estuaries to modulate hydrodynamics and alleviate sediment siltation problem, for example, the Changjiang Estuary, the Ems Estuary, and the Weser Estuary (Hesse et al. 2019; Hu et al. 2009; van Maren et al. 2015). An important difference in estuarine environments compared with coastal and riverine environments is the existence of a salinity gradient in both longitudinal and lateral directions. The longitudinal salinity gradient is important for gravitational circulation and is closely related to saltwater intrusion. Construction of groynes influences the geometry of the main channel, for example, the equivalent width or depth, which impacts channel hydrodynamics and possibly the degree of saltwater intrusion. Additionally, the salinity gradient complicates hydrodynamics in and around groyne fields, strengthening lateral flows and influencing sediment transport patterns (Chen et al. 2020; Chen and de Swart 2018; Zhou et al. 2019, 2021). Temporary storage of salt in the groyne fields during high tide generates a salinity gradient between the groyne fields and the main channel, which drives a near-bed flow toward the channel during low water slack. Our understanding of groyne effects in estuarine environments needs to be expanded because of the baroclinic processes.

The Changjiang Estuary in China provides an example of dikes and groynes within the transition zone between freshwater and salt water. Two 50-km-long dikes were constructed along both banks of the main navigation channel (North Passage), together with 1–2-km long groynes about every 5 km. The impact of the groynes on hydrodynamics and sediment transport was investigated by Zhou et al. (2019, 2021) using a realistic 3D numerical model. However, due to the bathymetric complexities, channel bends, and longitudinal variability of groyne size, it is difficult to identify the contribution of general and specific aspects of the groyne fields (length, width, depth, aspect ratio, and so on) in those studies. In this work, we aim to unravel the effects induced by groynes on (1) lateral exchange between groyne fields and the main channel, and (2) saltwater intrusion. For this aim, we set up an idealized hydrodynamic model in which we can systematically modify channel and groyne dimensions.

## Method

### An Idealized Model

An idealized model was developed using the Finite-Volume Community Ocean Model (FVCOM). FVCOM is a 3D primitive equation coastal ocean model with unstructured triangular grid in the horizontal and terrain-following  $\sigma$  coordinate in the vertical. It has been extensively used for hydrodynamics, sediment dynamics, and biogeochemistry studies in both complex geometries (Beardsley et al. 2013; Ge et al. 2015a, 2022; Shore 2009) and schematized environments (Wu et al. 2011). The overall accuracy of numerical scheme has been validated by Huang et al. (2008). In this study, an idealized model is developed to investigate the effect of groynes on hydrodynamics, especially on lateral flow and salinity transport, in a schematized tidal channel-shoal system (Fig. 1). The schematization of the geometry and hydrodynamic characteristics in the model are based on those of the North Passage, the main navigation route of the Changjiang Estuary [Fig. 1(a)].

The model domain includes a 300-km river channel ( $0 < x < 300$  km) and a  $120 \times 78$ -km<sup>2</sup> sea ( $300 < x < 420$  km,

$-39 < y < 39$  km) which includes a 90-km main channel ( $300 < x < 390$  km) with groyne fields on both sides [Fig. 1(b)]. Here, the main channel is defined as the area between north and south groyne tips, and the deep channel means the deepest flat part in the middle of the main channel. Two series of groynes with two long dikes are constructed in the model [Fig. 1(c)] with a lateral depth gradient in the groyne fields [Fig. 1(d)]. The dikes and groynes are treated as impermeable walls in FVCOM. This method has successfully resolved the geometrical structures and ambient flows around the dikes, groyne, or similar coastal defense constructions, from flume experiments to realistic cases (Ge et al. 2012, 2020; Wei et al. 2014). In the idealized experiments, the groynes and dikes are all set as walls without overtopping. The main channel width ( $B$ ) remains constant in this study (5 km) with a deep channel of constant width 1 km. The length of groyne ( $L$ ) can be adjusted. At the most upstream ( $x = 300$  km) and downstream ( $x = 390$  km) areas, there is no groyne.

The model uses unstructured grid including 63,546 triangular cells and 10 uniform  $\sigma$  layers in the vertical direction. A constant river discharge of 3,000 m<sup>3</sup>/s is applied at the upstream river boundary [Fig. 1(b)], uniformly flowing into the domain through all six cells at the river boundary. Tidal amplitudes and phases of eight major astronomical tidal constituents ( $M_2$ ,  $S_2$ ,  $N_2$ ,  $K_2$ ,  $K_1$ ,  $O_1$ ,  $P_1$ , and  $Q_1$ ), derived from model results of a well validated FVCOM model of the Changjiang Estuary (Ge et al. 2012, 2013, 2015b, 2020, 2022; Zhou et al. 2019, 2021), are specified at 15 nodes along the open sea boundary [Fig. 1(b)]. Specifically, the water elevation 30 km downstream from the end of the dikes in the Changjiang Estuary model is used for tidal analysis because it is also 30 km from the dike end to the sea boundary in this study.

Subsequently, these tidal amplitudes and phases are obtained and applied in the model. A salinity nudging boundary condition is applied at the downstream boundary with a target salinity specified as 35 psu, and a Blumberg and Kantha (1985) implicit radiation condition is used to calculate the perturbation of salinity. A semi-implicit solver is applied in this model using a time step of 12 s (with a spin-up time of 10 days) to avoid the adjustment between two-dimensional and three-dimensional models when using mode-split solver (Chen et al. 2013). It can provide better prediction of vertical salinity profiles and influenced saltwater intrusion.

In this model, the horizontal eddy viscosity is calculated following Smagorinsky (1963). Because the eddy viscosity is an important parameter for exchange flows between the main channel and the groyne fields, we have performed a sensitivity analysis on the horizontal mixing coefficient  $C$  in Smagorinsky eddy parameterization (Supplemental Materials), suggesting  $C$  only limitedly influences exchange flows. The vertical eddy viscosity, as well as the thermal/salt diffusion, are calculated using the Mellor-Yamada level 2.5 turbulent closure scheme (Mellor and Yamada 1982).

The bed level in the river channel is from  $-8$  m ( $x = 0$  km) to  $-12$  m ( $x = 300$  km). The bathymetry in the coastal area ( $x > 300$  km) becomes steeper along two gradients: (1) a 0.5-m increase of water depth in the groyne field area ( $300 < x < 390$  km), and (2) a 2.5-m increase in the offshore ( $390 < x < 420$  km). The depth of the deep channel ( $-12.5$  m in standard Case 0) can be adjusted by changing the slope from the groyne tip to the edge of the deep channel. The definition of model dimensions and relevant notations are summarized in Table 1. The dimensions of the groyne fields and the main channel of the standard case (Case 0) is shown in Fig. 1(d). The transverse area of the groyne field is  $1.5 \times 10^4$  m<sup>2</sup>, whereas that of the (half) channel [Fig. 1(d)] is  $2.675 \times 10^4$  m<sup>2</sup>.

The idealized model was developed with the aim to study effects of groyne fields on hydrodynamics in the channel-shoal system.

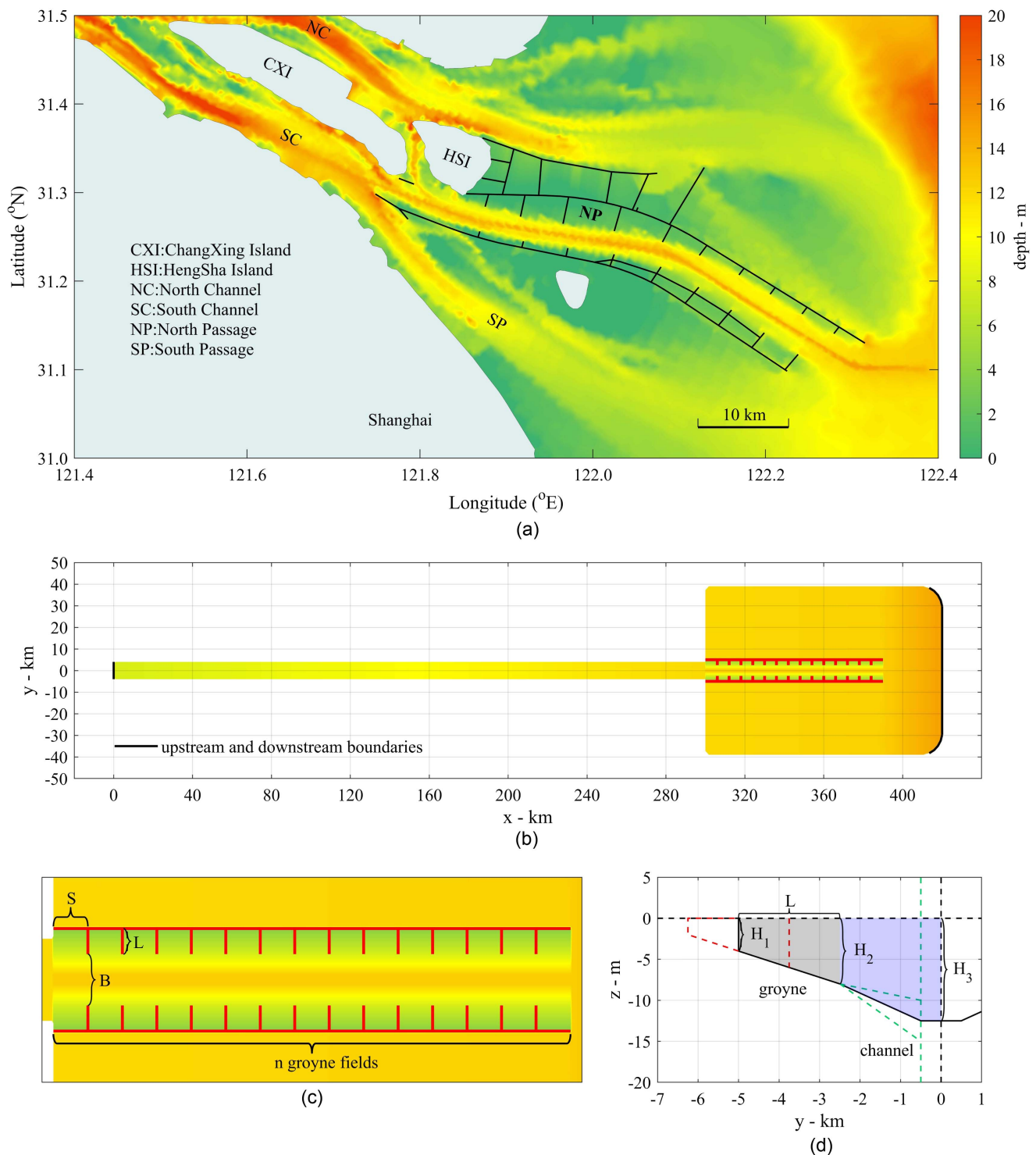


**Fig. 1.** (a) Bathymetry of the Changjiang Estuary and adjacent regions, where solid lines in the river mouth represent dikes and groynes around the North Passage; (b) model domain and bathymetry of the idealized model; (c) zoom-in view of the main channel with construction of dikes and groynes of the idealized model; and (d) bathymetry of cross-transverse in the main channel. Panels (a–c) share the same color bar.

Therefore, the dimensions of the groyne fields and the main channel are systematically adjusted for different scenarios. Within the centric area ( $300 < x < 390$  km,  $-8 < y < 8$  km), a right triangle with a resolution of 250 m is used, i.e., for the standard case (Case 0), there are 480 cells in a  $6,000 \times 2,500$ -m<sup>2</sup> groyne field. This resolution has been widely used in the North Passage (Ge et al. 2012, 2015b; Zhou et al. 2019, 2021). A sensitivity test on grid resolution (discussed in the Supplemental Materials) suggested

that the grid cell size starts influencing saltwater intrusion for values exceeding 250 m, but a value of 250 m still largely corresponds to smaller grid cell size results (the groyne fields in the North Passage are much larger than conventional groyne fields). Outside the centric area, the domain was discretized using varying triangular mesh, with a resolution varying from about 1,200 to 250 m in the river channel, and from about 250 to 6,500 m from the end of main channel to the open sea boundary.

**Table 1.** Dimension definition and notations in the model

Notation	Definition
$S$	Length of groyne field
$L$	Length of groyne
$B$	Width of the main channel (between two opposite groynes)
$n$	Number of groyne fields
$H_1$	Depth of groyne (at the groyne root)
$H_2$	Depth of groyne (at the groyne tip)
$H_3$	Depth of the deep channel

### Scenario Description

The effect of groynes is systematically investigated through nine model scenarios summarized in Table 2. Case 0 provides a reference case, which best represents the present-day North Passage of the Changjiang Estuary. Case 1 is set up to quantify the effect of salinity-driven exchange flows. Cases 2–7 have different distances between groynes while sharing the same length of groynes, providing a comparison on the effect of different aspect ratios of the groyne field. In this study, the aspect ratio is defined as  $S/L$  (ratio of the distance between adjacent groynes to the groyne length). Case 8 considers Coriolis force (using  $31^\circ$  N, the latitude of the Changjiang Estuary).

## Results

### Results of Reference Case

#### Water Level, Salinity, and Along-Channel Flow Velocity

Because this idealized model is based on the North Passage in the Changjiang Estuary, we compare results from our idealized model (reference Case 0) with the main hydrodynamic characteristics of the North Passage using observational data and a well-validated process-based model (Zhou et al. 2019, 2021).

The water levels in the main channel reveal a clear neap-spring tide variation [Fig. 2(a)] with a period of about 10 days. The maximum tidal range is about 2.6 m during spring tide. The tidal form factor [ $F = (K_1 + O_1)/(M_2 + S_2)$ ] calculated along a longitudinal transect in the channel is 0.26–0.29, indicating mainly semidiurnal tides, in agreement with the semidiurnal tides in the North Passage. Fig. 2 also shows preliminary results of the grid-resolution sensitivity test with resolutions of 125, 180, and 500 m, where a resolution of 250 m does not substantially differ in water elevation, salinity, or flow velocity from model realizations with a resolution less than 250 m.

**Table 2.** Scenario summary

Name	$S$ (km)	$L$ (km)	$S/L$	H1–H2 (m)	H3 (m)	Compared with Case 0
Case 0	6.0	2.5	2.4	4–8	12.5	—
Case 1	6.0	2.5	2.4	4–8	12.5	Barotropic
Case 2	1.0	2.5	0.4	4–8	12.5	Aspect ratio of groyne fields (number of groynes)
Case 3	2.5	2.5	1.0	4–8	12.5	
Case 4	5.0	2.5	2.0	4–8	12.5	
Case 5	7.5	2.5	3.0	4–8	12.5	
Case 6	10.0	2.5	4.0	4–8	12.5	
Case 7	—	—	—	4–8	12.5	
Case 8	6.0	2.5	2.4	4–8	12.5	(With) Coriolis force

Note: In all scenarios, the main channel width ( $B$ ) remains 5 km. Other notation is defined in Table 1.

Under a constant river discharge ( $3,000 \text{ m}^3/\text{s}$ ), the salinity variation is in dynamic equilibrium, varying over the tidal cycle and over the spring-neap cycle but without an apparent decreasing/increasing trend. Over the spring-neap cycle, the salinity varies between 8 and 20 psu in the surface layer, and 13 and 22 psu in the bottom layer [Fig. 2(b)]. During neap tides (Days 10–12), the salinity variation was relatively small compared with other periods. Moreover, the difference of salinity between surface and bottom layers is also much larger during neap tides. These stratified neap tidal conditions reflect stronger saltwater intrusion during neap tides, in agreement with the situation in the North Passage.

The computed bottom along-channel velocity is in the range of about  $-1.1$  to  $1.0 \text{ m/s}$  [Fig. 2(c)], which agrees with the typical along-channel velocity in the North Passage (Lin et al. 2021; Zhou et al. 2021). The surface along-channel velocity is ebb-dominant, whereas the bottom along-channel velocity is slightly flood-dominant. This vertical variation of current velocity results from salinity-driven gravitational circulation.

### Stratification

A bulk Richardson number ( $R_{ib}$ ) is used to quantify stratifying and mixing conditions as follows:

$$R_{ib} = \frac{gD\Delta\rho}{\bar{\rho}_w|\bar{u}_s^2|} \quad (1)$$

where  $D$  = water depth;  $\Delta\rho$  = bottom-surface density difference;  $\bar{\rho}_w$  = vertically averaged density; and  $\bar{u}_s$  = surface current velocity. A high  $R_{ib}$  [ $\log_{10}(R_{ib}/0.25) > 0$ ] indicates strong stratification (and lower values indicate mixing). During high-water slack (HWS), the whole channel is strongly stratified, and stratification is more pronounced in the deep channel and around groyne tips [Fig. 3(a)]. The main channel becomes well-mixed during peak ebb, but the groyne fields remain highly stratified [Fig. 3(b)]. During low-water slack (LWS), the groyne fields are vertically well-mixed, except at the interface between the groyne fields and the main channel [Fig. 3(c)]. The strong stratification along the interface is induced by salinity-induced shoal-to-channel (STC) lateral flow (with salt water from the groyne field being transported to the main channel as a near-bed density current). In the main channel, there is a transition between mixing and stratifying conditions from upstream to downstream. During peak flood, the main pattern of stratification is similar to that during peak ebb [Fig. 3(d)], although mixing in the main channel is weaker and stratification in the groyne fields is stronger compared with peak ebb. The patterns of stratification in Fig. 3 show high similarity with the stratification distribution in the North Passage reported by Zhou et al. (2021) in the following aspects: (1) the order of magnitude of  $R_{ib}$ , (2) the spatial patterns of  $R_{ib}$  (especially the difference between the groyne fields and the main channel) at characteristic time periods, and

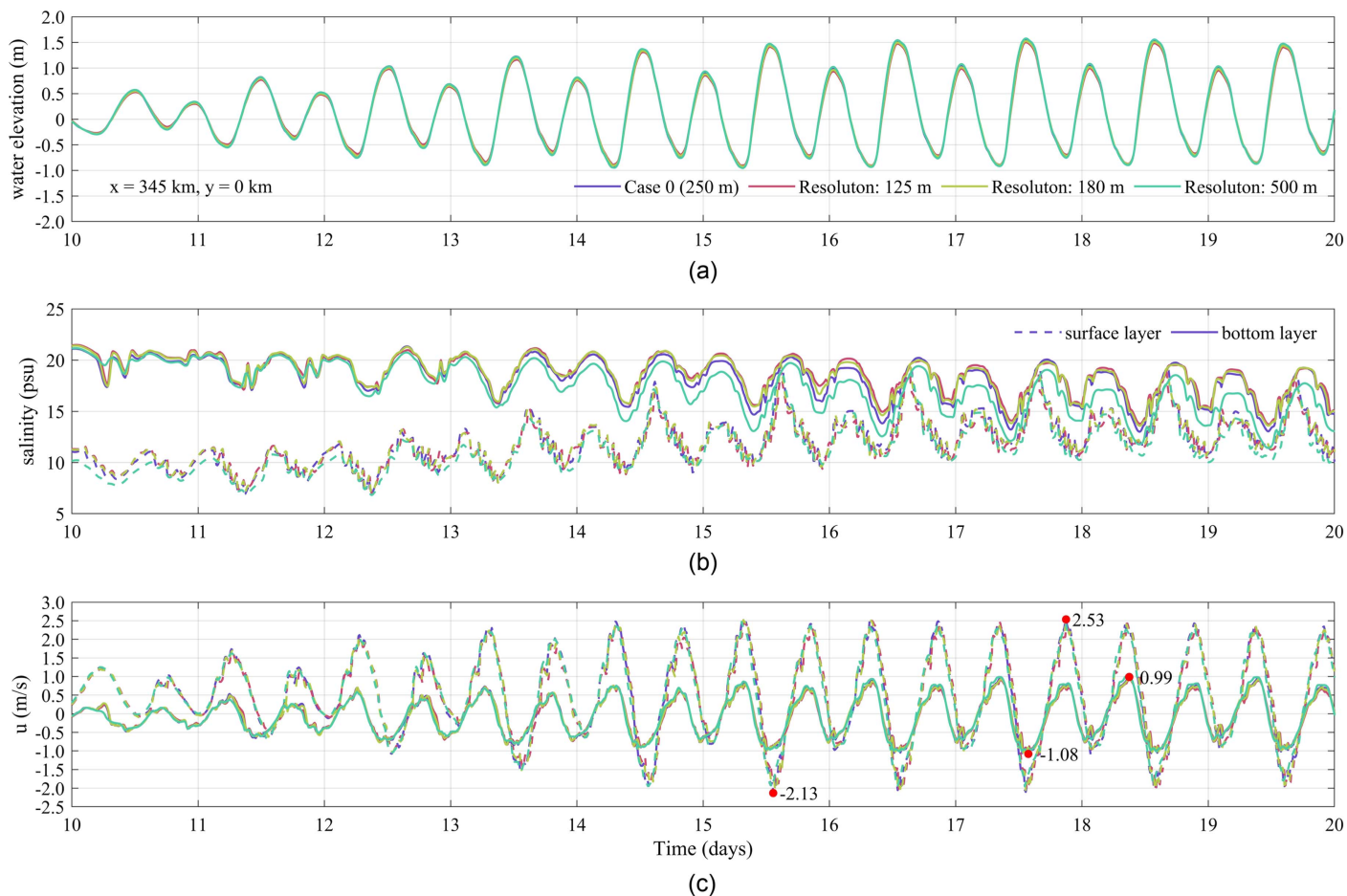


**Fig. 2.** (a) Water elevations; (b) surface and bottom salinity; and (c) surface and bottom flow velocity at the middle of the main channel ( $x = 345$  km,  $y = 0$  km) in Case 0 with four grid resolutions. Typical velocities are marked in panel (c).

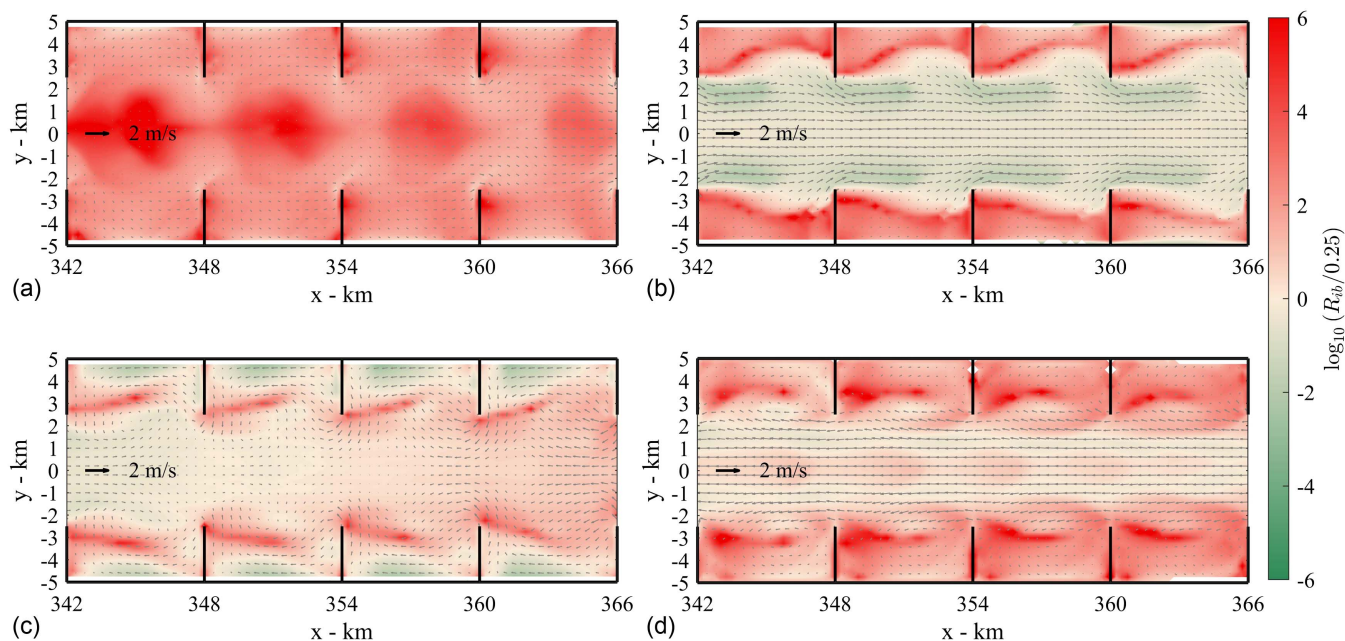


**Fig. 3.** Distribution of bulk Richardson number [ $\log_{10}(R_{ib}/0.25)$ ] and velocity vectors in the channel for (a) high-water slack [Case 0, Day 13 - 02:40:00 (HWS)]; (b) peak ebb currents [Case 0, Day 13 - 06:20:00 (peak ebb)]; (c) low-water slack [Case 0, Day 13 - 08:20:00 (LWS)]; and (d) peak flood currents [Case 0, Day 13 - 12:40:00 (peak flood)]. High-water slack and low-water slack conditions are based on flow velocity reversal. Results are from Case 0.

(3) the strong stratification around the groyne tips during LWS. These similarities further suggest that the idealized model captures the major characteristics of the North Passage, Changjiang Estuary. A more detailed comparison is given in the Supplemental Materials.

### Lateral Flow and Effects of Salinity

During moderate and the following spring tides, the retention of salt water in groyne fields during ebb leads to pronounced lateral flows during low-water slacks. Shoal-to-channel density-induced lateral flows may occur or be enhanced, especially in the bottom layer of water column. To further investigate lateral flow and potential effects on mass exchange between groyne fields and the main channel, results of bottom lateral current velocities from Case 0 during moderate tide at four characteristic time periods are shown in Fig. 4. The lateral velocities are presented in a converging direction, i.e., positive for shoal-to-channel (STC) currents and negative for channel-to-shoal (CTS) currents.

In this section, we use a north groyne field, where  $354 < x < 360$  km, to illustrate lateral flows in the bottom layer [Fig. 4(a)]. During HWS, STC lateral currents with a velocity between 0.1 and 0.2 m/s occur upstream of the groynes, whereas the other parts are dominated by channel-to-shoal (CTS) currents [Fig. 4(a)]. For the weak hydrodynamic conditions around HWS, these transverse flows are relatively small. During peak ebb currents, stronger lateral flows (0.2–0.4 m/s) exist both landward and seaward of the groynes, and CTS currents exist in the main channel [Fig. 4(b)]. During LWS, significant bottom STC currents occur seaward of the groynes, with a maximum velocity exceeding 0.7 m/s [Fig. 4(c)]. This result agrees with findings by Zhou et al. (2019, 2021).

Effects of salinity gradient joint with existence of groynes result in asymmetric lateral flows during HWS and LWS. During peak flood currents [Fig. 4(d)], the lateral flows are relatively weak, similar to the period with peak ebb currents. Fig. 4 indicates an obvious difference of bottom lateral flows related to the relative position in

groyne fields to groynes. Therefore, lateral flows on three cross-channel transects in the groyne field at different positions (1 km downstream to a groyne, at the middle of a groyne field, and 1 km upstream to a groyne) are shown in Fig. 5 [Fig. 4(a) shows a plan view position of these transects].

During HWS, a STC pattern is observed in the groyne field at the surface layer, with a progressive increase in magnitude (from 0.05 to 0.4 m/s) [Figs. 5(a, e, and i)]. CTS currents occur at greater depths and in most areas in the main channel. During the following ebb maximum, STC currents (0.1–0.2 m/s) dominate in the groyne field in Transect A (whole water column) [Fig. 5(b)], whereas Transect B is mainly characterized by CTS currents [Fig. 5(f)] and a lateral circulation structure can be found in Transect C [Fig. 5(j)]. During LWS, the groyne field and the low-water column in the main channel have strong STC currents (up to 0.4 m/s) in Transect A [Fig. 5(c)]. In Transects B and C, CTS currents dominate [Figs. 5(g and k)]. During peak flood currents, Transects A and B have weak CTS currents with a magnitude below 0.2 m/s [Figs. 5(d and h)], whereas STC currents occur in Transect C [Fig. 5(l)]. The pattern of lateral flows during flood maximum shows a consistency with the pattern of HWS.

The lateral flows and channel-shoal water exchange are strongly influenced by groyne fields and salinity gradients. Effects of salinity gradients are shown in Fig. 6. During the ebb period, salt is kept in the groyne fields due to retention effects of groynes [Figs. 6(a and b)]. Then, the salinity gradient between the groyne fields and the main channel drives the lateral flow during LWS [Fig. 6(c)]. Fig. 6(d) shows the transport of salt into the groyne fields. In the barotropic case (Case 1), the lateral flow during LWS is much lower compared with Case 0 (not shown here).

### Horizontal Eddy Structure

The idealized model reflects the formation and breakdown of a horizontal eddy structure in the groyne field. Here, we take the bottom layer as an example (Fig. 7). At 02:40 (HWS), the streamlines

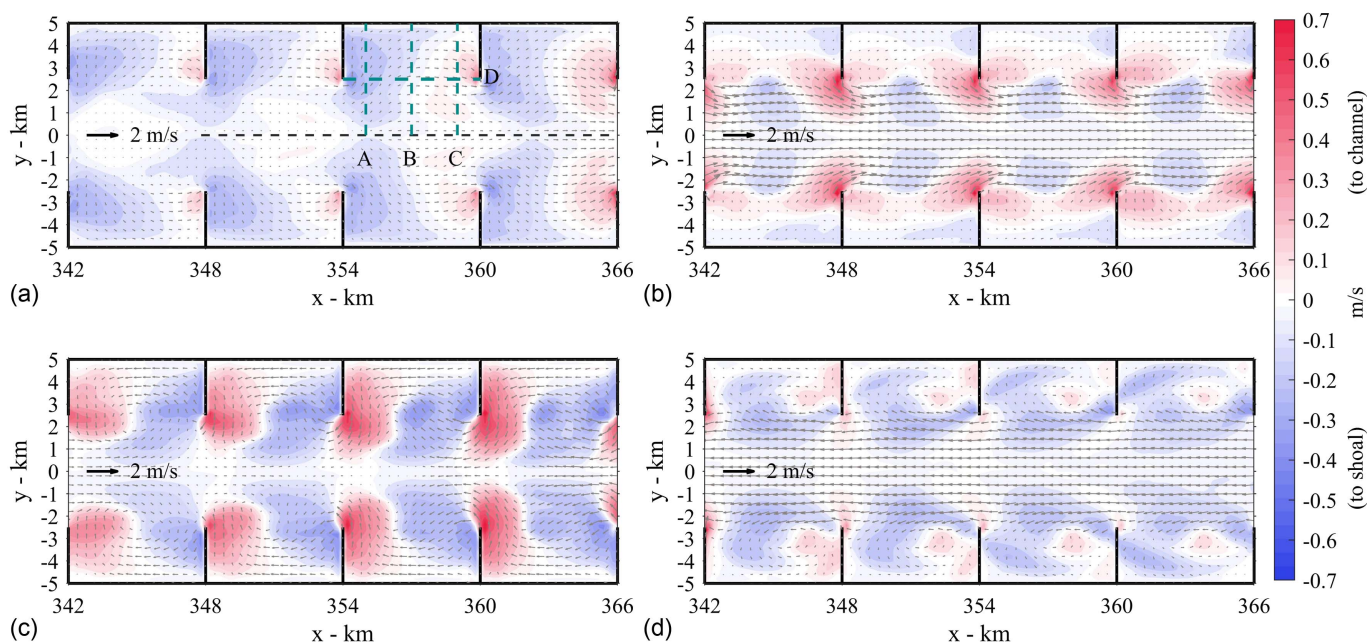


**Fig. 4.** Bottom lateral current velocities and velocity vectors at (a) HWS [Case 0, Day 13 - 02:40:00 (HWS)]; (b) ebb maximum [Case 0, Day 13 - 06:20:00 (peak ebb)]; (c) LWS [Case 0, Day 13 - 08:20:00 (LWS)]; and (d) flood maximum [Case 0, Day 13 - 12:40:00 (peak flood)]. A positive value indicates a direction from groyne fields to the main channel (STC, from both sides). These results are from Case 0 in moderate tidal conditions. Three cross-channel and one along-channel transects are marked with dashed lines.

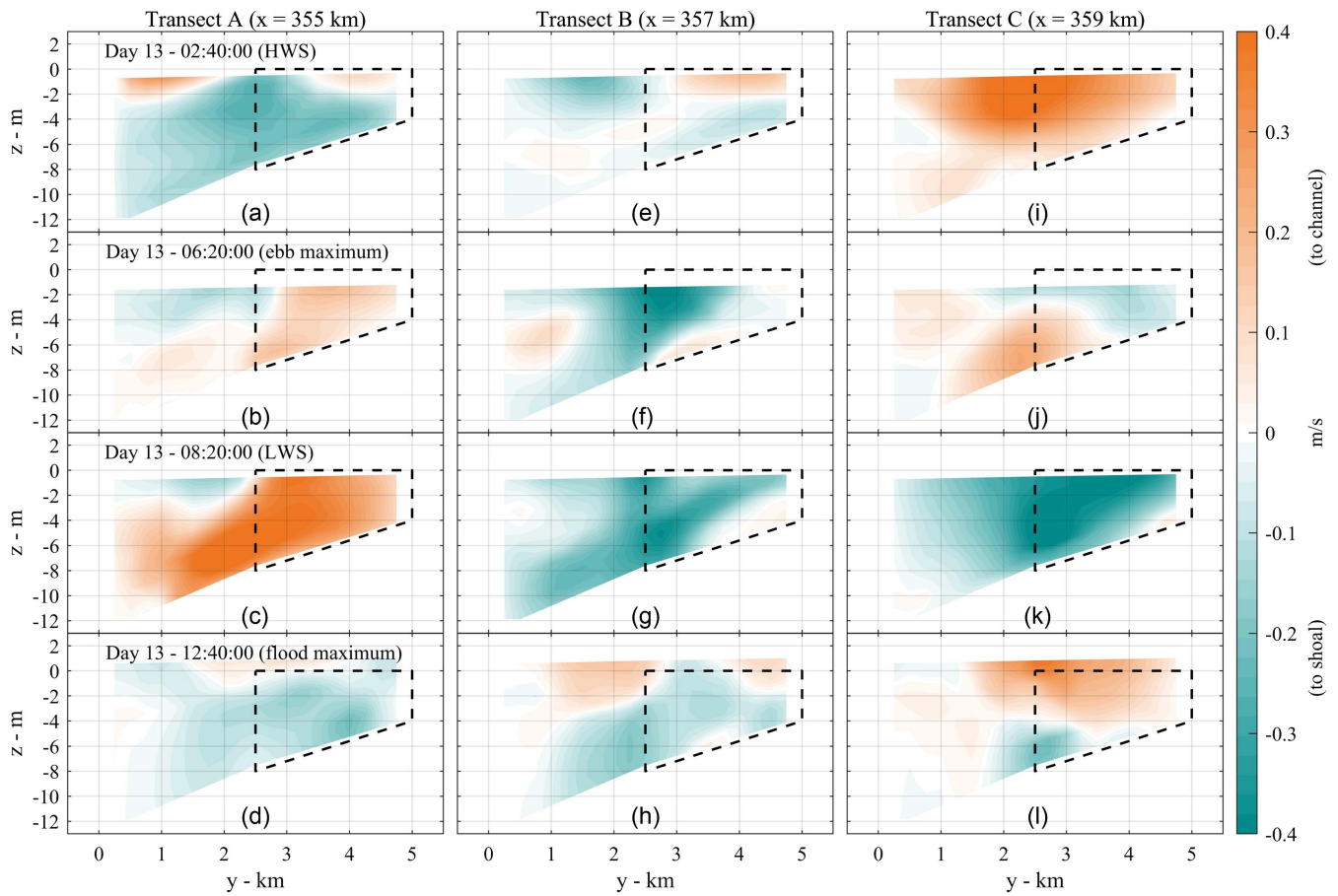


**Fig. 5.** Lateral flows on three cross-channel transects in Case 0: (a–d) Transect A at  $x = 355$  km (1 km downstream to a groyne): (a) Day 13 - 02:40:00 (HWS); (b) Day 13 - 06:20:00 (ebb maximum); (c) Day 13 - 08:20:00 (LWS); and (d) Day 13 - 12:40:00 (flood maximum); (e–h) Transect B at  $x = 357$  km (at the middle of a groyne field); and (i–l) Transect C at  $x = 359$  km (1 km upstream to a groyne) at (a, e, and i) HWS; (b, f, and j) ebb maximum; (c, g, and k) LWS; and (d, h, and l) flood maximum. The four time periods are identical with those in Fig. 4. Dashed lines indicate position of groynes.

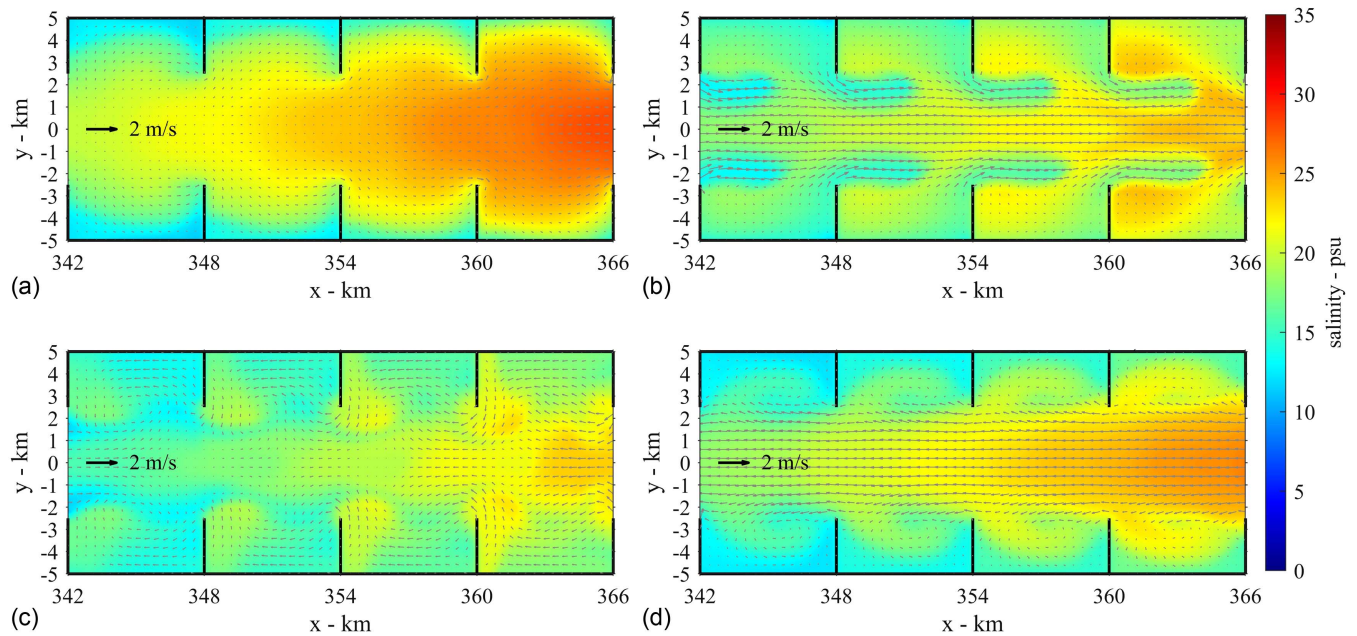


**Fig. 6.** Bottom salinity distribution in Case 0 at four moments corresponding to time periods in Fig. 4: (a) HWS (Day 13 - 02:40:00); (b) peak ebb (Day 13 - 06:20:00); (c) LWS (Day 13 - 08:20:00); and (d) peak flood (Day 13 - 12:40:00).

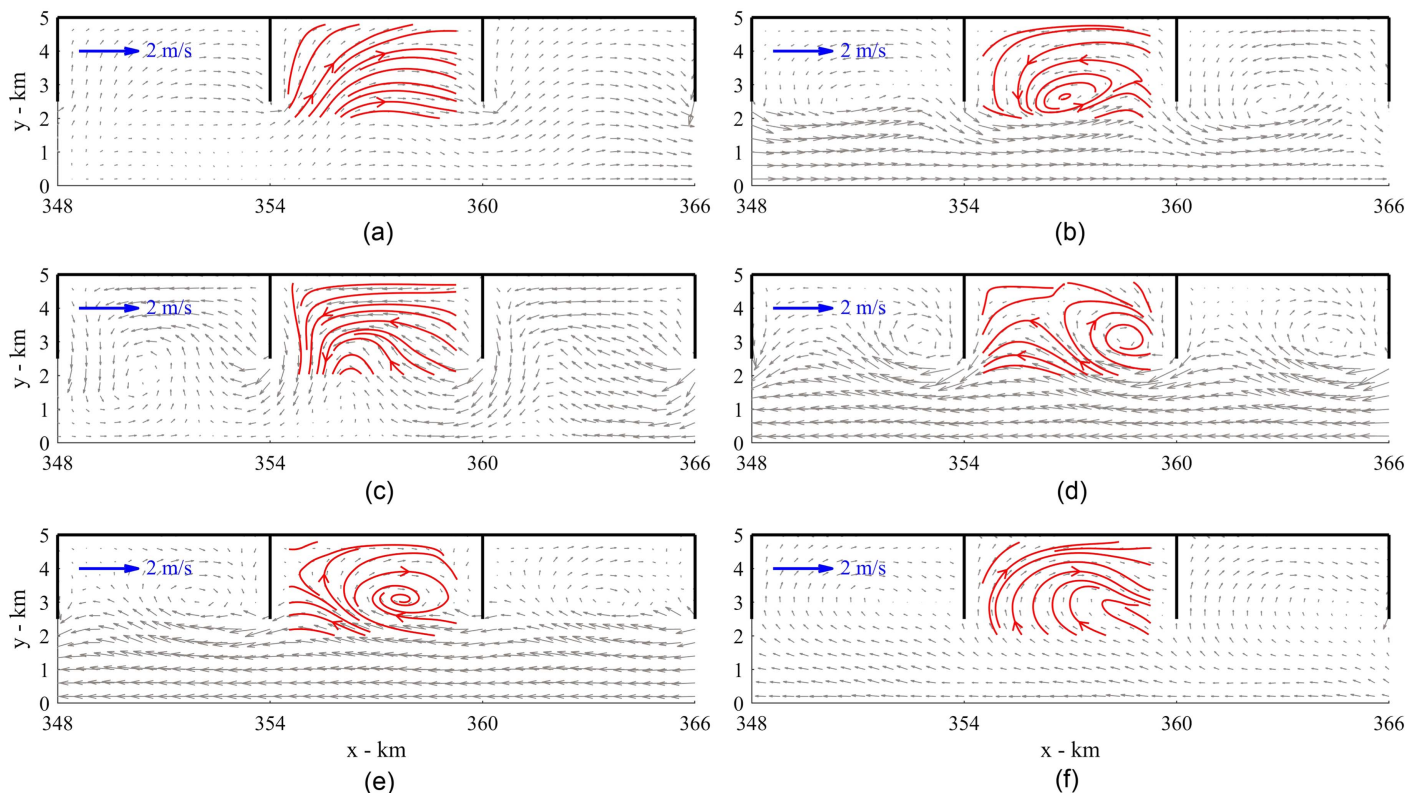


**Fig. 7.** Velocity vectors (gray arrows) in the main channel and streamlines (lines) in the groyne field during moderate tides at (a) 02:40:00 (high-water slack); (b) 07:00:00; (c) 08:20:00 (low-water slack); (d) 11:00:00; (e) 12:00:00; and (f) 14:40:00 in Day 13. Other arrows are length scales for velocity vectors. Velocity data are from the bottom layer of Case 0.

indicate that weak ebb currents enter the groyne field but flow out of the groyne field without the development of a pronounced eddy structure [Fig. 7(a)]. A pronounced eddy develops in the groyne field at 07:00 during the ebb period [Fig. 7(b)]. Near the end of the ebb period, the streamlines show similarity with those during HWS [Fig. 7(c)]. Figs. 7(d–f) illustrate a process of formation, extension, and breakdown of an eddy during the flood period. The streamlines' pattern is periodic, and after 14:40 [Fig. 7(f)], a new cycle starts with an eddy similar to that during HWS [Fig. 7(a)].

The eddy structure in the groyne field featured a primary eddy and dynamic eddy near the groyne tip. The dynamic eddy mainly occurs at the beginning of ebb and flood processes (not shown in Fig. 7). The eddy structure presented here is not the same as that in the laboratory experiments of Uijtewaal et al. (2001), lacking a secondary eddy. The main reason for this difference is the effect of roughness in the groyne field. In laboratory experiments, the water depth (a few centimeters) in shoal areas are much smaller than the setting in our idealized model (and in the groyne fields in the Changjiang Estuary) and therefore, frictional effects in the laboratory experiments are larger than that in our idealized model. In the model, the drag coefficient  $C_d$  is calculated as follows:

$$C_d = \max \left( \frac{k^2}{\ln \left( \frac{z_{ab}}{z_0} \right)^2}, cbcmin \right) \quad (2)$$

where  $z_{ab}$  = height above the bottom;  $k = 0.4$  is the von Karman constant; and bottom roughness parameter  $z_0 = 8 \times 10^{-5}$  m to achieve similar flow velocities comparable to in situ velocities in the North Passage while keeping the convergence and stability of

the model; and the minimum bottom roughness  $cbcmin = 5 \times 10^{-5}$ , which is small enough to ensure a  $z_0$ -calculated  $C_d$ .

### Scenario Comparison

#### Tidal Propagation

Construction and different layouts of groynes are expected to influence tidal propagation. These tidal modulations by groyne field layouts need to be known to understand more detailed hydrodynamics within the channel such as channel-shoal exchange processes. The effects of groynes on tidal propagation are therefore investigated using Cases 2–7 (and the reference Case 0).

The major velocity of the  $M_2$  tide [computed using the T-Tide toolbox version 1.3 (Pawlowicz et al. 2002)] near the outlet of the main channel ( $x = 405$  km) is about 1.1 m/s. Just seaward of the channel ( $x$  from 405 to 390 km), the tidal velocity decreases due to flow resistance effects induced by the landward located dikes and groynes (Fig. 8). The flow velocity increases again ( $x$  from 390 to 380 km) within the channel enveloped by groynes, due to flow contraction. Halfway the main channel ( $x$  from 350 to 320 km) the  $M_2$  velocity amplitude slightly increases again for scenarios with a small groyne field aspect ratio (Case 2 and 3). The fluctuation in Cases 4–6 is directly related to the aspect ratio, i.e., at locations where groynes are constructed, there is an increase of velocity because the channel is locally narrowed by groynes.

Case 7 is an extreme case without any groyne in the channel, which essentially corresponds to a widened channel and a situation before construction of groynes. This results in a smaller tidal velocity in the channel, but a larger velocity in the up-estuary tidal river (Fig. 8). Case 7 demonstrates that the construction of groynes

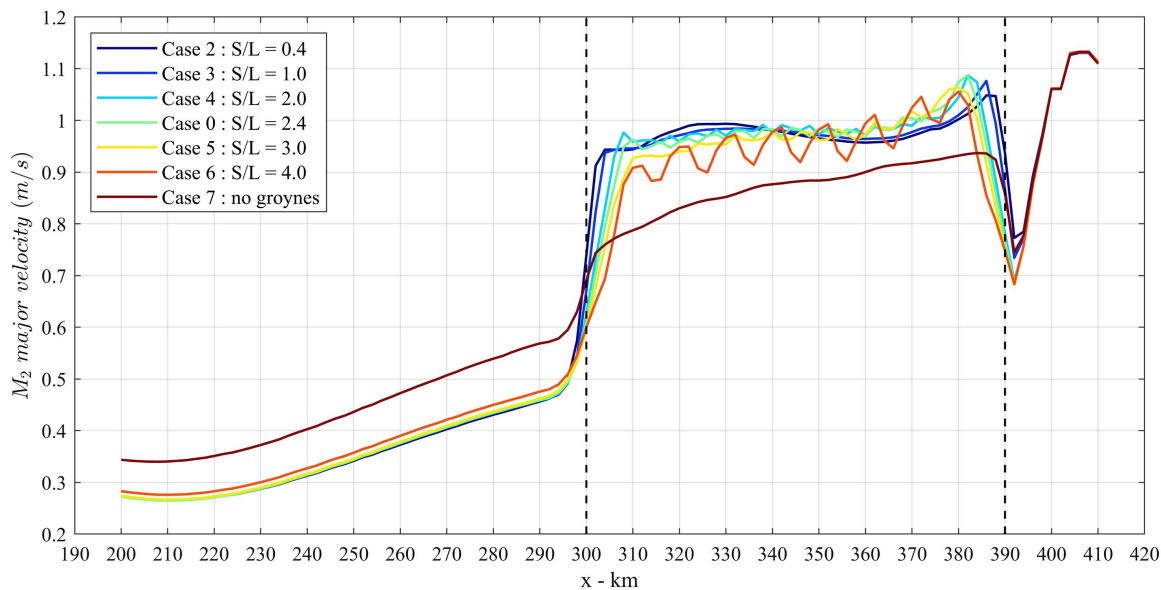


**Fig. 8.** Longitudinal distribution of major velocity of  $M_2$  tide in scenarios with different numbers of groynes, by harmonic analysis for depth-averaged longitudinal velocity. Dashed lines indicate the upstream and downstream boundaries of the channel.

modulated the velocity distribution in the whole system, including the velocity increase in the main channel. This agrees with the common designing purpose of groynes in a navigational channel, i.e., to maintain channel depth by increasing the current velocity.

#### Effects of Aspect Ratio

To quantify water exchange between the groyne field and the main channel, a decomposition method (Vanlede and Dujardin 2014) was used in this study (details are given in the Supplemental Materials)

$$v(x, z, t) = v_{\text{tidal}} + v_{\text{hor}} + v_{\text{ver}} + v_{\text{res}} \quad (3)$$

The cross-transverse velocity [i.e.,  $v(x, z, t)$  in the  $y$ -axis direction] can be decomposed into (1) tidal filling and emptying ( $v_{\text{tidal}}$ ), (2) the horizontal component of cross-channel exchange ( $v_{\text{hor}}$ , inflow and outflow in the  $x$ - $y$  plane), which has no variation over the vertical, (3) the vertical component of cross-channel exchange ( $v_{\text{ver}}$ , inflow and outflow in the  $y$ - $z$  plane), which has no variation over the horizontal, and (4) a residual component ( $v_{\text{res}}$ ), respectively. These parameters reflect the channel-shoal exchange mechanisms in response to groyne field dimensions. The aspect ratio can affect the eddy structure in groyne fields (Sukhodolov et al. 2002; Uijtewaal 2005; Uijtewaal et al. 2001) and determine the amount of salt that can be transported into and stored in groyne fields. Therefore, the aspect ratio may have a considerable impact on channel-shoal exchange, from both vertical- and horizontal-circulation perspectives.

For different aspect ratios, the cross-sectional areas where exchange between a groyne field and the main channel take place differ in size, and therefore the total exchange flux cannot be used for a scenario comparison. As a result,  $v_{\text{ver}}$  and  $v_{\text{hor}}$  are used to discuss effects of aspect ratio on lateral exchange. For each scenario, a groyne field to conduct the calculation is determined by the averaged salinity in the groyne field from Day 10 to Day 25 (averaged over both time and volume).

The water level is provided in Fig. 9(a) for reference to the tidal cycle. Here,  $v_{\{\text{hor},\text{out}\}}$  and  $v_{\{\text{ver},\text{out}\}}$  represent the outflowing  $v_{\text{hor}}$  and  $v_{\text{ver}}$  from the groyne field to the main channel. It was found that  $v_{\{\text{hor},\text{out}\}}$  is stronger for a larger aspect ratio [Fig. 9(b)].

The maximum  $v_{\{\text{hor},\text{out}\}}$  was about 0.23 m/s in all scenarios. In particular,  $v_{\{\text{hor},\text{out}\}}$  was obviously smaller (about 0.17 m/s) for the smallest aspect ratio (Case 3) compared with other scenarios. The positive correlation between the aspect ratio and  $v_{\{\text{hor},\text{out}\}}$  is also reflected in the time-averaged value (Table 3). During both flood and ebb periods,  $v_{\{\text{hor},\text{out}\}}$  decreased as the aspect ratio decreased, indicating a smaller aspect ratio can constrain the horizontal exchange.

For the vertical component  $v_{\text{ver}}$ ,  $v_{\{\text{ver},\text{out}\}}$  and the net  $v_{\text{ver}}$  showed opposite patterns compared with  $v_{\text{hor}}$  [Figs. 9(c) and d)]. A smaller aspect ratio can lead to a larger peak of  $v_{\{\text{ver},\text{out}\}}$  (about 0.09 m/s) at the end of flood tide [Fig. 9(c)]. However, the net  $v_{\text{ver}}$  was smaller compared with other scenarios [Fig. 9(d)], indicating that a smaller aspect ratio can lead to stronger cross-channel vertical circulation, i.e., inflow (in the surface layer) and outflow (in the bottom layer) are all stronger with a smaller aspect ratio. This is also evident from values of  $v_{\text{ver}}$  averaged over the flood and ebb period (Table 3): a smaller aspect ratio strengthens gravitational circulation in the lateral direction. This inverse influence of the aspect ratio on  $v_{\text{ver}}$  and  $v_{\text{hor}}$  is probably related to the impact of  $v_{\text{hor}}$  on residence times. With a large aspect ratio, the horizontal flow component is large and salt water is flushed out of the groyne field by horizontal flows. This weakens the transverse salinity gradient between the main channel and the groyne fields, and consequently the salinity-driven vertical exchange flows. For smaller aspect ratios, salt water needs to be flushed out by gravitational currents.

In summary, aspect ratio can cause opposite effects on horizontal exchange and gravitational circulation. A small aspect ratio can enhance gravitational circulation but prohibit horizontal exchange. Although the horizontal component is usually much larger than the vertical component (Fig. 9 and Table 3), the vertical effects may be amplified when calculating the transport of materials that have a vertical gradient of concentrations, for example, the suspended sediment. More investigation is needed, and caution should be taken when designing the aspect ratio.

#### Effects of Coriolis Force

Coriolis force can influence salinity transport and lateral exchange in the channel-shoal system. The influence is from two aspects:

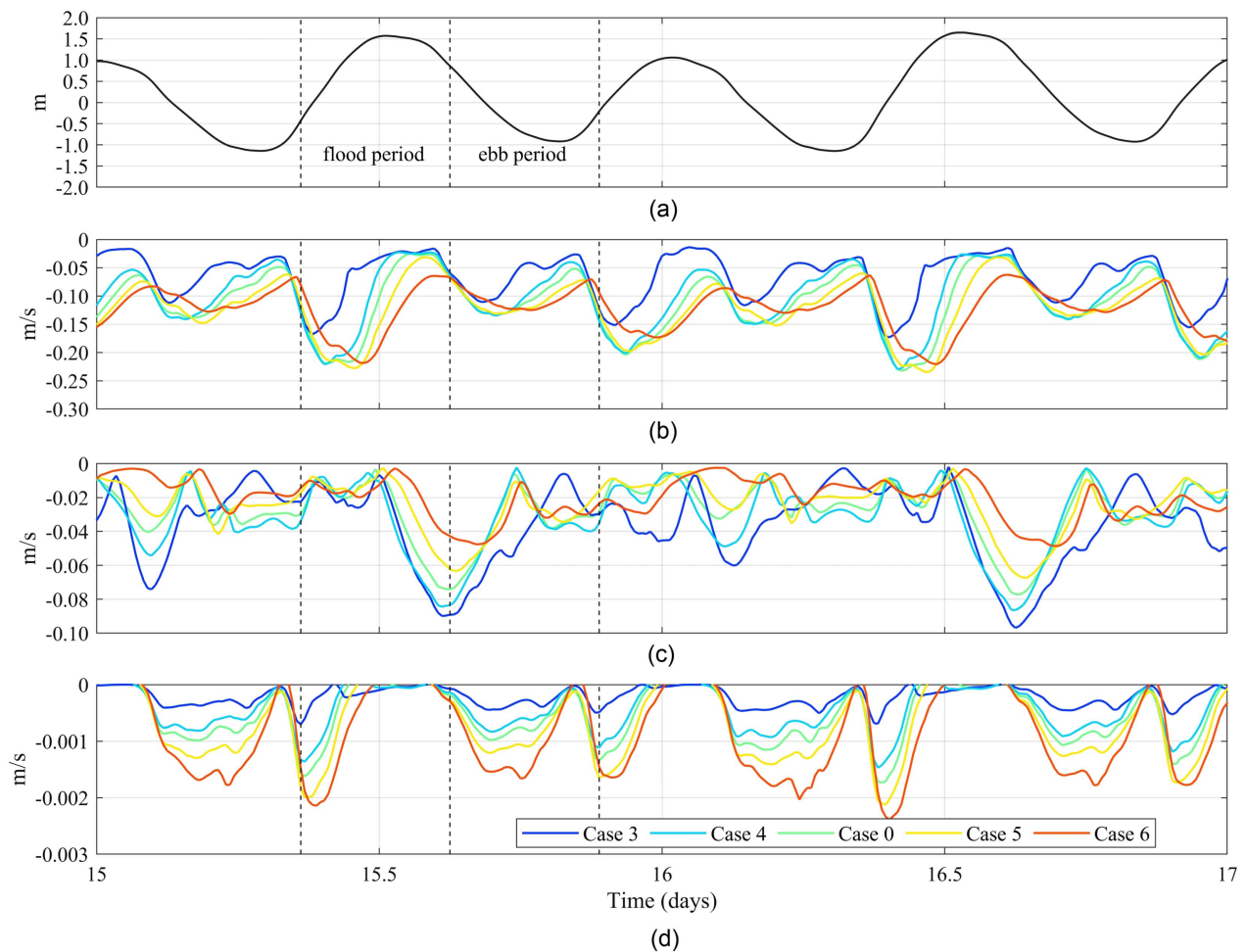


**Fig. 9.** (a) Water level in Case 0 averaged on an along-channel transect [Transect D in Fig. 4(a)]; (b) horizontal component of exchange velocity, outflowing from a groyne field to the main channel in different scenarios (for each scenario, the specific groyne field has a downstream groyne at  $x = 360$  km) ( $v_{\text{hor,out}}$ ); (c) vertical component, similar to panel (b) ( $v_{\text{ver,out}}$ ); and (d) net vertical component of exchange velocity across the interface between a groyne field and the main channel (net  $v_{\text{ver}}$ ).

**Table 3.** Average value of outflowing horizontal component, outflowing vertical component, and net vertical component of exchange velocity on the flood and ebb periods, respectively

Case	Aspect ratio	$v_{\text{hor,out}}$ (m/s)		$v_{\text{ver,out}}$ (m/s)		Net $v_{\text{ver}}$ ( $\times 10^{-4}$ m/s)	
		Flood	Ebb	Flood	Ebb	Flood	Ebb
3	1.0	-0.066	-0.067	-0.036	-0.044	-1.15	-2.75
4	2.0	-0.106	-0.092	-0.034	-0.039	-2.23	-5.17
0	2.4	-0.120	-0.099	-0.029	-0.037	-2.73	-6.39
5	3.0	-0.136	-0.106	-0.021	-0.035	-3.88	-7.99
6	4.0	-0.145	-0.103	-0.017	-0.033	-5.73	-9.61

(1) the difference caused by Coriolis force compared with the standard case, and (2) the asymmetry induced by Coriolis force between the north and south groyne fields. Therefore, a groyne field on the north side in Case 8 and two symmetric groyne fields in Case 8 (with Coriolis force) are compared in terms of tidal filling-induced exchange velocity and the vertical component of exchange velocity (the horizontal component is mainly determined by the aspect ratio, and effects of Coriolis force are limited from both aspects mentioned previously). For groyne fields on the north side, a positive value of the exchange velocity represents inflowing

velocity, whereas for groyne fields on the south side (Fig. 10), it represents outflowing velocity.

In Case 8, the Coriolis force causes stronger inflowing velocity induced by tidal filling on the north groyne field compared with the south groyne field [Fig. 10(b)]. However, for Cases 0 and 8, the Coriolis force shows negligible effect on the north side groyne field. The Coriolis force obviously decreases  $v_{\text{ver,out}}$  in the north groyne field, especially during neap tide [Fig. 10(c)]. However, the Coriolis force results in a larger  $v_{\text{ver,out}}$  on the south side, forming a significant asymmetry between the north and south sides.

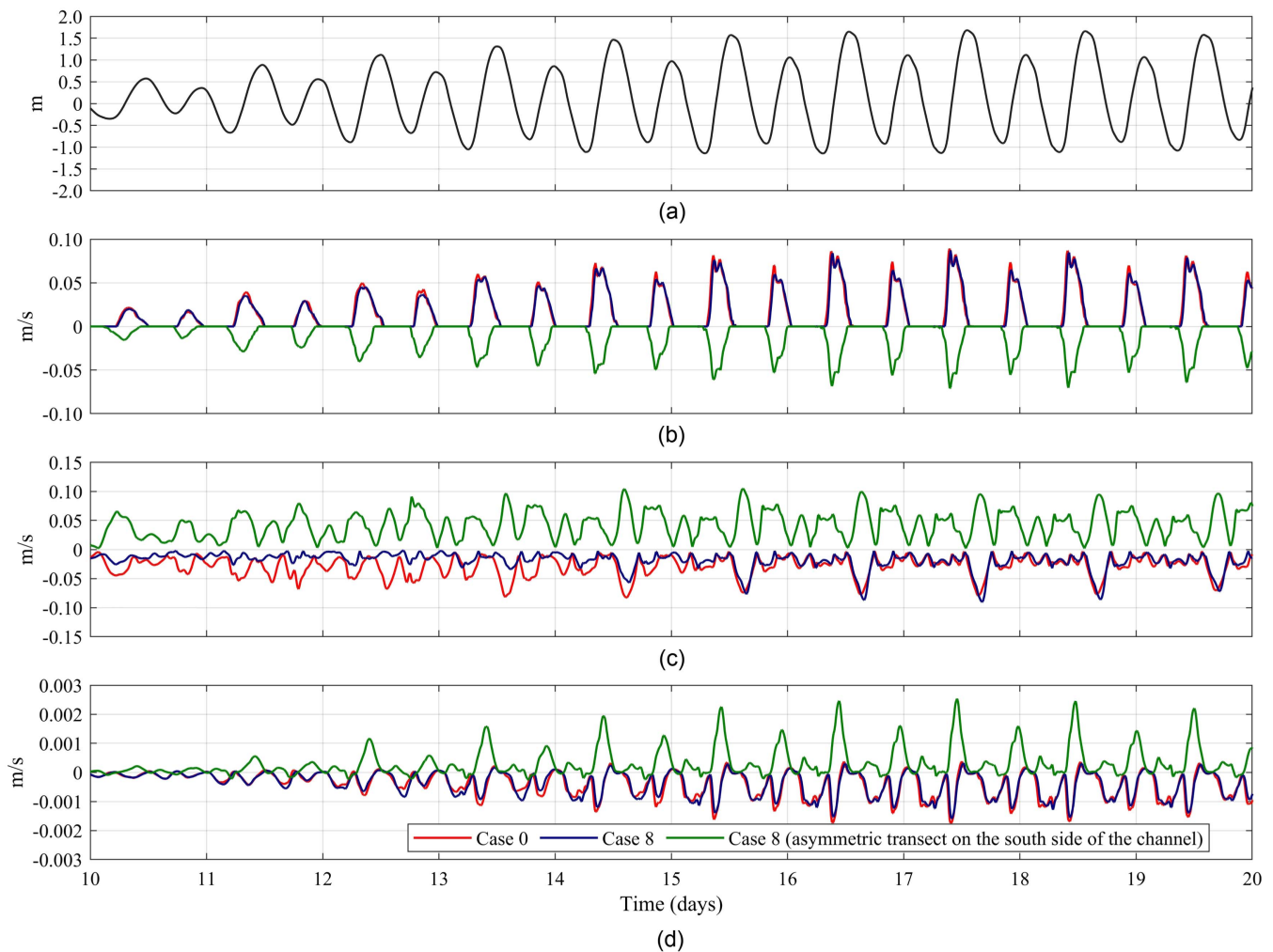


**Fig. 10.** (a) Water level in Case 0 averaged on an along-channel transect [Transect D in Fig. 4(a)]; (b) tidal filling component of exchange velocity, inflowing from the main channel to groyne fields ( $v_{\text{tidal,in}}$ ); (c) vertical component of exchange velocity outflowing from groyne fields to the main channel ( $v_{\text{ver,out}}$ ); and (d) net vertical component of exchange velocity (net  $v_{\text{ver}}$ ).

**Table 4.** Average value of inflowing tidal filling component, outflowing vertical component, and net vertical component of exchange velocity during neap tide (Days 11 and 12) and spring tide (Days 15 and 16)

Case	Location	$v_{\text{tidal,in}}$ (m/s)		$v_{\text{ver,out}}$ (m/s)		Net $v_{\text{ver}}$ ( $\times 10^{-4}$ m/s)	
		Neap	Spring	Neap	Spring	Neap	Spring
0	North	0.009	0.018	-0.032	-0.029	-1.61	-5.09
8	North	0.009	0.017	-0.012	-0.022	-1.82	-4.81
8	South	-0.007	-0.012	0.037	0.046	1.14	4.02

This asymmetry is more significant during neap tides; the daily averaged  $v_{\text{ver,out}}$  is about twice as large on the south side than on the north side (Table 4).

For the net  $v_{\text{ver}}$ , the difference between Cases 0 and 8 is relatively small [Fig. 10(d)]. Although the highest values of the net  $v_{\text{ver}}$  is larger in the southern groyne field, the second peak (during ebb tide) is much smaller, resulting in a smaller daily-averaged net  $v_{\text{ver}}$  (Table 4). These findings illustrate that for large-scale groyne fields (several kilometers), such as those in the Changjiang Estuary, Coriolis force introduces a substantial difference in exchange mechanisms along the south and north banks.

### Saltwater Intrusion

Because groynes strongly influence channel hydrodynamics, they also influence saltwater intrusion. In this section, we compare saltwater intrusion for scenarios with different groyne configurations (Cases 2–7, including Case 0). The degree of saltwater intrusion is represented with the 1-psu contour line in Fig. 11. From Figs. 11(a–n), the amount of groynes decreases. The saltwater intrusion first increases with a decreasing amount of groynes [Figs. 11(a–c and h–j)], but decreases again when the amount of groynes further decreases [Figs. 11(d–g and k–n)] in both neap and spring tidal conditions. These results indicated that (1) the amount

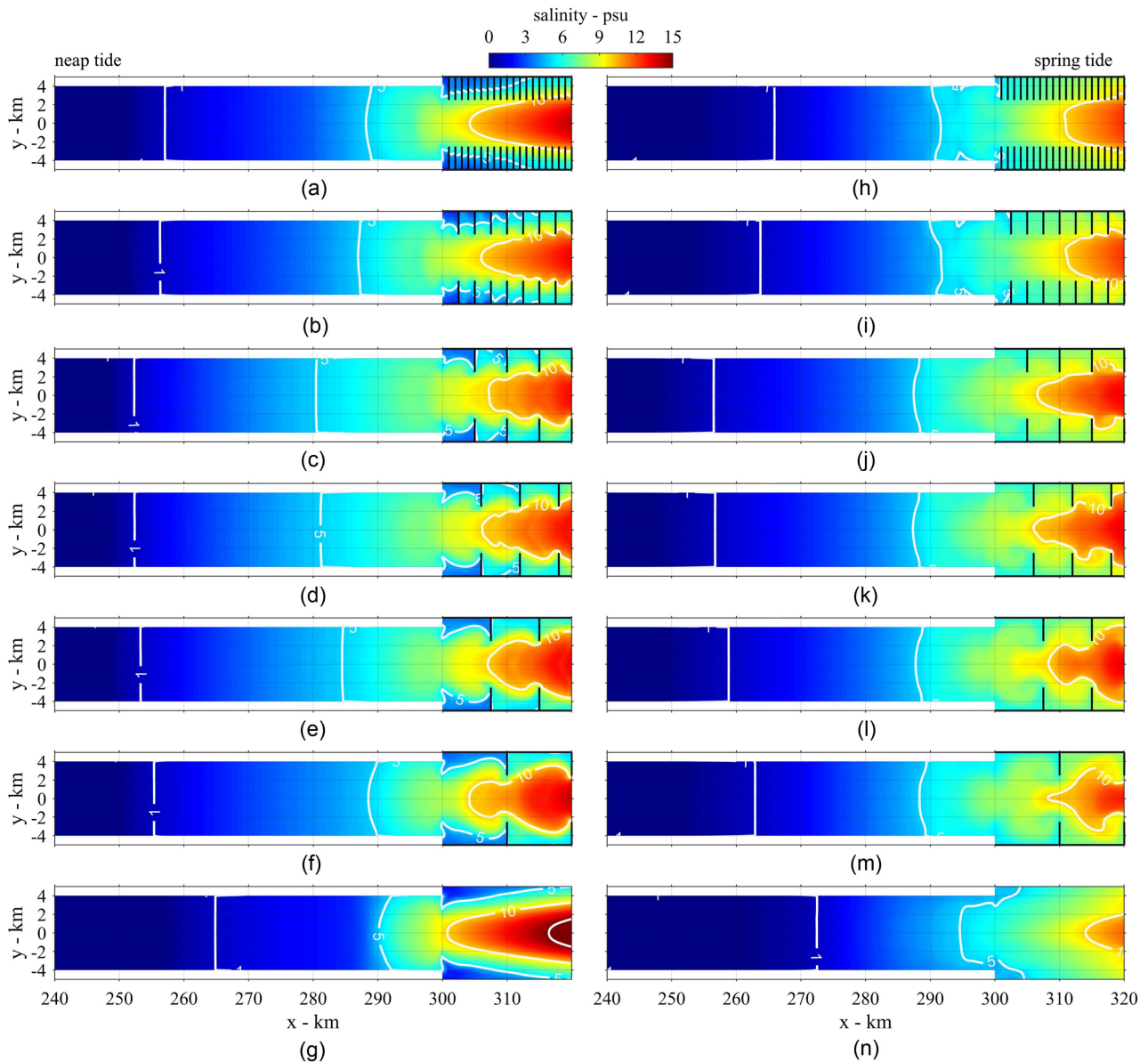


**Fig. 11.** Saltwater intrusion in different scenarios during neap tide and spring tide. Contour lines of 1, 5, 10, and 15 psu in the bottom layer are shown with open lines: (a) Case 2, time = 11 03:00:00, S/L = 0.4; (b) Case 3, time = 11 03:00:00, S/L = 1; (c) Case 4, time = 11 03:00:00, S/L = 2; (d) Case 0, time = 11 03:00:00, S/L = 2.4; (e) Case 5, time = 11 03:00:00, S/L = 3; (f) Case 6, time = 11 03:00:00, S/L = 4; (g) Case 7, time = 11 03:00:00; (h) Case 2, time = 15 04:30:00, S/L = 0.4; (i) Case 3, time = 15 04:30:00, S/L = 1; (j) Case 4, time = 15 04:30:00, S/L = 2; (k) Case 0, time = 15 04:30:00, S/L = 2.4; (l) Case 5, time = 15 04:30:00, S/L = 3; (m) Case 6, time = 15 04:30:00, S/L = 4; and (n) Case 7, time = 15 04:30:00.

of groynes has a nonlinear effect on saltwater intrusion, and (2) a specific number of groynes exists for which saltwater intrusion is maximal.

The difference of saltwater intrusion between neap tides and spring tides is reflected most clearly by high-salinity contour lines (Fig. 11). During neap tides, the 10-psu contour lines show an opposite pattern compared with the 1-psu contour lines (minimal intrusion for intermediate aspect ratios). However, during spring tides, the 1- and 10-psu contour lines are more consistent in terms of intruding distance. This is illustrated more clearly in Fig. 12. The most significant saltwater intrusion occurs when 12–18 groynes are constructed on each side of the channel, corresponding to aspect ratio about 2.0–3.0. This is opposite for the 10- and 15-psu salinity contour lines computed during neap tides (Fig. 12).

Summarizing, it is demonstrated that groynes influence the saltwater intrusion. Groynes may enhance saltwater intrusion with 12.8

to 16.0 km (for neap to spring tides) compared with Case 7 (without any groyne).

## Discussion

### Effects of Groynes on Saltwater Intrusion: Tidal Dynamics

The effects of groynes on tidal propagation was evaluated for the  $M_2$  and  $S_2$  tides. Groynes substantially increased tidal velocities in the channel, compared with the nongroyne case [Figs. 13 (a and b)]. The aspect ratio (also the number of groynes) nonlinearly influenced the degree of velocity increase, in agreement with the nonlinear effects on saltwater intrusion shown in Fig. 12. The  $S_2$  tide was most strongly influenced by the aspect ratio in

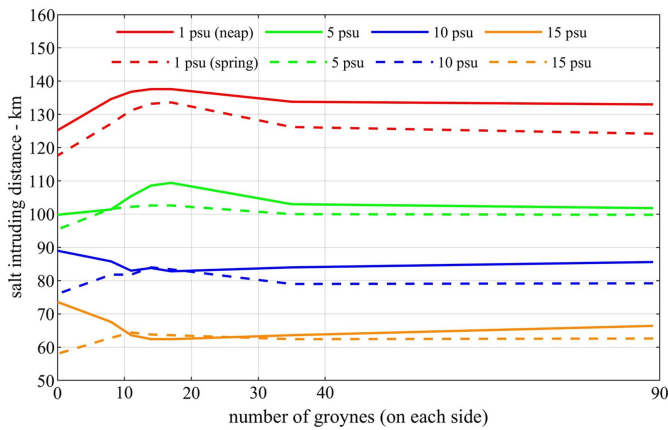


**Fig. 12.** Intruding distance of different salinity contour lines in conditions of different groyne numbers. Intruding distance is the distance from the seaward end of the channel ( $x = 390$  km) to the position of each contour line. Solid and dashed lines indicate the intrusion in spring and neap cycles, respectively.

Cases 4, 0, and 5 (aspect ratio = 2.0, 2.4, and 3.0, respectively). The major velocities of the  $S_2$  tide increased more strongly (relative to the nongroyne case) than that of the  $M_2$  tide (Fig. 13). The combinations of the  $M_2$  and  $S_2$  tides therefore introduce a dependence of tidal propagation during neap and spring tides on the aspect ratio. During neap tides, intermediate aspect ratios (2.0–3.0) resulted in the lowest velocities, whereas during spring tides, intermediate aspect ratios led to the highest velocities [Fig. 13(c)].

### Effects of Groynes on Saltwater Intrusion: Mixing and Stratification

In this study, the idealized model also showed stronger saltwater intrusion during neap tides. Because the salinity distribution is closely related to mixing and stratification in the channel, we further analyzed the stability of the water column. For this purpose the

logarithmic bulk Richardson number [ $\log_{10}(R_{ib}/0.25)$ ] was spatially averaged for each part of the channel-shoal system to show an overall level of stratification in the river, the main channel, and the groyne fields, respectively (Fig. 14).

During neap tides, the whole system was more strongly stratified than during spring tides (Fig. 14). Vertical mixing in the main channel was most pronounced for aspect ratios from 2.0 to 4.0, corresponding to more pronounced saltwater intrusion as well [Fig. 14(b)]. This indicates that during neap tides, saltwater intrusion scales with vertical mixing rates in the main channel (and not to flow velocities, which are lowest during these conditions). During spring tides, mixing rates were higher (compared with the neap tides) but are also less dependent on the aspect ratio [Fig. 14(b)].

### General Implications and Future Work

For environments characterized by unidirectional flows and limited salinity gradient, such as the Rhine River researched by Yossef and de Vriend (2010), the groyne fields experienced a net sediment import that led to filled-up groyne fields as an equilibrium state. However, the dynamic equilibrium state is affected by multiple processes, e.g., ship navigation-induced sediment export (Ten Brinke et al. 2004). The equilibrium is also influenced by human interventions in the main channel, where intense dredging in the main channel may weaken the channel-to-shoal net transport. This study focused on the groyne-induced lateral effects in a tide-dominated estuary, where salinity gradients and cross-currents play a crucial role. Consistent with Yossef and de Vriend (2010), the primary circulation cell dominated the flow and salinity transport patterns in the groyne field, showing opposite directions during ebb and flood periods. However, salinity-induced shoal-to-channel flows were asymmetric during tidal cycles, thereby potentially influencing net sediment transport. Furthermore, near-bed high-concentration sediment can further affect the density gradient, therefore complicating the flow asymmetry. We recommend executing future model-based studies that incorporate sediment dynamics to explore how groynes impact residual sediment transport through cross-shore exchange flows and a modified longitudinal salinity distribution.

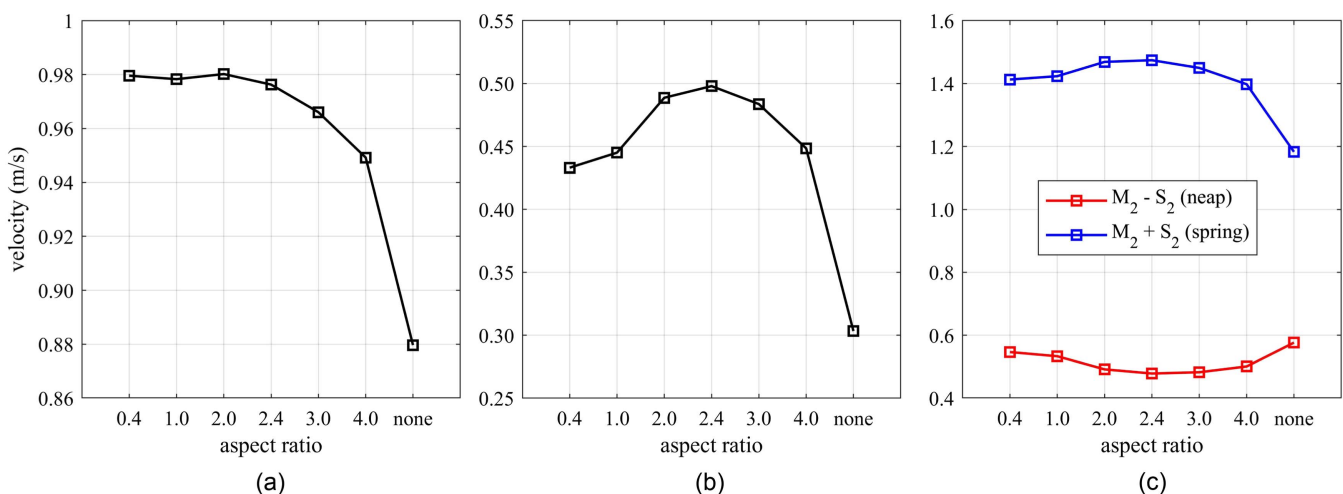


**Fig. 13.** Averaged major velocity of (a)  $M_2$ ; (b)  $S_2$ ; and (c) subtraction and summation of  $M_2$  and  $S_2$  from  $x = 310$  to  $390$  km. Results of  $M_2$  are the same as the results in Fig. 8, and results of  $S_2$  were obtained with the same method used for the  $M_2$  tide.

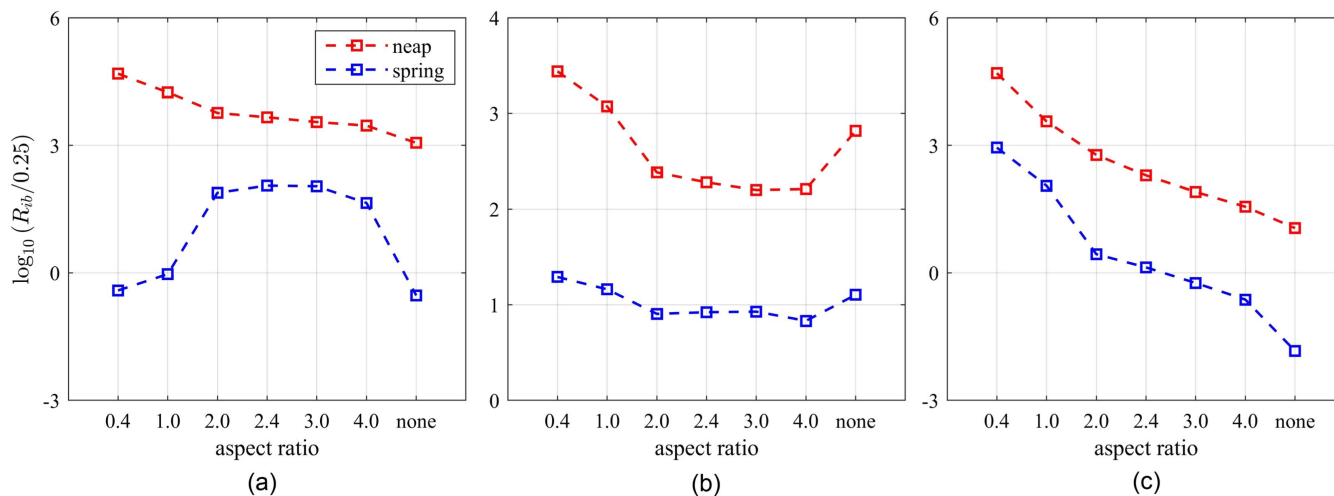


Fig. 14. Spatially averaged  $\log_{10}(R_{ib}/0.25)$  in (a) river; (b) main channel; and (c) groyne field.

## Conclusion

This study set out to explore the impacts of groynes constructed in estuarine environments on hydrodynamics, channel-shoal exchange, and saltwater intrusion. In addition to their longitudinal effects, groynes in estuaries also exert significant influence on lateral flow and channel-shoal exchange.

Due to the retention effect of groynes on salt water during the early ebb, higher salinity in groyne fields will increase density-driven lateral flows from groyne fields to the main channel during the late ebb. The salinity gradient causes an asymmetry of lateral currents during ebb and flood periods, for example, enhancing lateral flow during low-water slack and weakening that during high-water slack. When combined with the presence of high mass concentration such as suspended sediment near the seabed, these factors significantly influence the overall mass transport, making lateral mass transport in a channel-shoal system more complicated in estuarine environments compared with riverine environments.

This study also revealed that saltwater intrusion does not linearly scale with the numbers of groynes (or aspect ratio of the groyne field). Groynes impact both tidal dynamics (by influencing horizontal dispersion) and vertical mixing (by influencing vertical dispersion and density-driven flows), which jointly determine the degree of saltwater intrusion in the channel-shoal system. Specifically, horizontal dispersion is more dominant during spring tidal conditions, whereas vertical dispersion is more important during neap tidal conditions. Saltwater intrusion is maximal for intermediate aspect ratios, which is the result of an optimum in vertical mixing during neap tides and an optimum in horizontal shear dispersion during spring tides. The findings also demonstrated that a smaller aspect ratio constrains horizontal exchange by eddies but enhances lateral gravitational circulation; the opposite was observed for a large aspect ratio. The Coriolis force can introduce substantial variability in exchange mechanisms on the south and north banks of the channel on the scale of a system such as the North Passage and other similar estuarine channels.

## Data Availability Statement

All data, models, or code that support the findings of this study are available from the corresponding author upon reasonable request.

## Acknowledgments

This research is supported by the National Key R&D Program of China (Grant No. 2022YFE0117500), the National Natural Science Foundation of China (Grant No. 41776104), and KNAW Project (Grant PSA-SA-E-02).

## Supplemental Materials

Appendixes S1–S4 are available online in the ASCE Library ([www.ascelibrary.org](http://www.ascelibrary.org)).

## References

- Beardsley, R. C., C. Chen, and Q. Xu. 2013. "Coastal flooding in Scituate (MA): A FVCOM study of the 27 December 2010 nor'easter." *J. Geophys. Res.: Oceans* 118 (11): 6030–6045. <https://doi.org/10.1002/2013JC008862>.
- Biron, P. M., C. Robson, M. F. Lapointe, and S. J. Gaskin. 2005. "Three-dimensional flow dynamics around deflectors." *River Res. Appl.* 21 (9): 961–975. <https://doi.org/10.1002/rra.852>.
- Blumberg, A. F., and L. H. Kantha. 1985. "Open boundary condition for circulation models." *J. Hydraul. Eng.* 111 (2): 237–255. [https://doi.org/10.1061/\(ASCE\)0733-9429\(1985\)111:2\(237\)](https://doi.org/10.1061/(ASCE)0733-9429(1985)111:2(237)).
- Chen, C., R. C. Beardsley, G. Cowles, J. Qi, Z. Lai, G. Gao, D. Stuebe, Q. Xu, P. Xue, and J. Ge. 2013. *An unstructured grid, finite-volume Community Ocean model FVCOM user manual*. SMASST/UMASSD Technical Rep. No. 13-0701. Dartmouth, MA: School of Marine Science and Technology, Univ. of Massachusetts-Dartmouth.
- Chen, L., W. Gong, H. Zhang, L. Zhu, and W. Cheng. 2020. "Lateral circulation and associated sediment transport in a convergent estuary." *J. Geophys. Res.: Oceans* 125 (8): e2019JC015926. <https://doi.org/10.1029/2019jc015926>.
- Chen, W., and H. E. de Swart. 2018. "Longitudinal variation in lateral trapping of fine sediment in tidal estuaries: Observations and a 3D exploratory model." *Ocean Dyn.* 68 (3): 309–326. <https://doi.org/10.1007/s10236-018-1134-z>.
- Ge, J., C. Chen, J. Qi, P. Ding, and R. C. Beardsley. 2012. "A dike-groyne algorithm in a terrain-following coordinate ocean model (FVCOM): Development, validation and application." *Ocean Modell.* 47 (Jan): 26–40. <https://doi.org/10.1016/j.ocemod.2012.01.006>.
- Ge, J., C. Chen, Z. B. Wang, K. Ke, J. Yi, and P. Ding. 2020. "Dynamic response of the fluid mud to a tropical storm." *J. Geophys. Res.: Oceans* 125 (3): e2019JC015419. <https://doi.org/10.1029/2019JC015419>.

- Ge, J., P. Ding, and C. Chen. 2015a. "Low-salinity plume detachment under non-uniform summer wind off the Changjiang Estuary." *Estuarine Coastal Shelf Sci.* 156 (Apr): 61–70. <https://doi.org/10.1016/j.ecss.2014.10.012>.
- Ge, J., P. Ding, C. Chen, S. Hu, G. Fu, and L. Wu. 2013. "An integrated East China Sea–Changjiang Estuary model system with aim at resolving multi-scale regional–shelf–estuarine dynamics." *Ocean Dyn.* 63 (Aug): 881–900. <https://doi.org/10.1007/s10236-013-0631-3>.
- Ge, J., J. Lu, J. Zhang, C. Chen, A. Liu, and P. Ding. 2022. "Saltwater intrusion-induced flow reversal in the Changjiang Estuary." *J. Geophys. Res.: Oceans* 127 (11): e2021JC018270. <https://doi.org/10.1029/2021JC018270>.
- Ge, J., F. Shen, W. Guo, C. Chen, and P. Ding. 2015b. "Estimation of critical shear stress for erosion in the Changjiang Estuary: A synergy research of observation, GOCI sensing and modeling." *J. Geophys. Res.: Oceans* 120 (12): 8439–8465. <https://doi.org/10.1002/2015JC010992>.
- Glas, M., K. Glock, M. Tritthart, M. Liedermann, and H. Habersack. 2018. "Hydrodynamic and morphodynamic sensitivity of a river's main channel to groyne geometry." *J. Hydraul. Res.* 56 (5): 714–726. <https://doi.org/10.1080/00221686.2017.1405369>.
- Hesse, R. F., A. Zorndt, and P. Fröhle. 2019. "Modelling dynamics of the estuarine turbidity maximum and local net deposition." *Ocean Dyn.* 69 (Apr): 489–507. <https://doi.org/10.1007/s10236-019-01250-w>.
- Hu, K., P. Ding, Z. Wang, and S. Yang. 2009. "A 2D/3D hydrodynamic and sediment transport model for the Yangtze Estuary, China." *J. Mar. Syst.* 77 (1–2): 114–136. <https://doi.org/10.1016/j.jmarsys.2008.11.014>.
- Huang, H., C. Chen, G. W. Cowles, C. D. Winant, R. C. Beardsley, K. S. Hedstrom, and D. B. Haidvogel. 2008. "FVCOM validation experiments: Comparisons with ROMS for three idealized barotropic test problems." *J. Geophys. Res.: Oceans* 113 (C7): 1–14. <https://doi.org/10.1029/2007JC004557>.
- Lin, J., B. C. van Prooijen, L. Guo, C. Zhu, Q. He, and Z. B. Wang. 2021. "Regime shifts in the Changjiang (Yangtze River) Estuary: The role of concentrated benthic suspensions." *Mar. Geol.* 433 (Mar): 106403. <https://doi.org/10.1016/j.margeo.2020.106403>.
- McCoy, A., G. Constantinescu, and L. Weber. 2007. "A numerical investigation of coherent structures and mass exchange processes in channel flow with two lateral submerged groynes." *Water Resour. Res.* 43 (5): 1–26. <https://doi.org/10.1029/2006WR005267>.
- Mellor, G. L., and T. Yamada. 1982. "Development of a turbulence closure model for geophysical fluid problems." *Rev. Geophys.* 20 (4): 851–875. <https://doi.org/10.1029/RG020i004p00851>.
- Ouillon, S., and D. Dartus. 1997. "Three-dimensional computation of flow around groyne." *J. Hydraul. Eng.* 123 (11): 962–970. [https://doi.org/10.1061/\(ASCE\)0733-9429\(1997\)123:11\(962\)](https://doi.org/10.1061/(ASCE)0733-9429(1997)123:11(962)).
- Pawlowicz, R., B. Beardsley, and S. Lentz. 2002. "Classical tidal harmonic analysis including error estimates in MATLAB using T\_TIDE." *Comput. Geosci.* 28 (8): 929–937. [https://doi.org/10.1016/S0098-3004\(02\)00013-4](https://doi.org/10.1016/S0098-3004(02)00013-4).
- Shore, J. A. 2009. "Modelling the circulation and exchange of Kingston Basin and Lake Ontario with FVCOM." *Ocean Modell.* 30 (2–3): 106–114. <https://doi.org/10.1016/j.ocemod.2009.06.007>.
- Smagorinsky, J. 1963. "General circulation experiments with the primitive equations." *Mon. Weather Rev.* 91 (3): 99–164. [https://doi.org/10.1175/1520-0493\(1963\)091<0099:GCEWTP>2.3.CO;2](https://doi.org/10.1175/1520-0493(1963)091<0099:GCEWTP>2.3.CO;2).
- Sukhodolov, A., W. S. J. Uijttewaalt, and C. Engelhardt. 2002. "On the correspondence between morphological and hydrodynamical patterns of groyne fields." *Earth Surf. Processes Landforms* 27 (3): 289–305. <https://doi.org/10.1002/esp.319>.
- Ten Brinke, W. B. M., F. H. Schulze, and P. van Der Veer. 2004. "Sand exchange between groyne-field beaches and the navigation channel of the Dutch Rhine: The impact of navigation versus river flow." *River Res. Appl.* 20 (8): 899–928. <https://doi.org/10.1002/rra.809>.
- Tritthart, M., M. Liedermann, and H. Habersack. 2009. "Modelling spatio-temporal flow characteristics in groyne fields." *River Res. Appl.* 25 (1): 62–81. <https://doi.org/10.1002/rra.1169>.
- Uijttewaalt, W. S. 2005. "Effects of groyne layout on the flow in groyne fields: Laboratory experiments." *J. Hydraul. Eng.* 131 (9): 782–791. [https://doi.org/10.1061/\(ASCE\)0733-9429\(2005\)131:9\(782\)](https://doi.org/10.1061/(ASCE)0733-9429(2005)131:9(782)).
- Uijttewaalt, W. S. J., D. Lehmann, and A. van Mazijk. 2001. "Exchange processes between a river and its groyne fields: Model experiments." *J. Hydraul. Eng.* 127 (11): 928–936. [https://doi.org/10.1061/\(ASCE\)0733-9429\(2001\)127:11\(928\)](https://doi.org/10.1061/(ASCE)0733-9429(2001)127:11(928)).
- Vanlede, J., and A. Dujardin. 2014. "A geometric method to study water and sediment exchange in tidal harbors." *Ocean Dyn.* 64 (Nov): 1631–1641. <https://doi.org/10.1007/s10236-014-0767-9>.
- van Maren, D. S., T. van Kessel, K. Cronin, and L. Sittioni. 2015. "The impact of channel deepening and dredging on estuarine sediment concentration." *Cont. Shelf Res.* 95 (Mar): 1–14. <https://doi.org/10.1016/j.csr.2014.12.010>.
- Wei, E., A. Zhang, Z. Yang, Y. Chen, J. Kelley, F. Aikman, and D. Cao. 2014. "NOAA's nested northern Gulf of Mexico operational forecast systems development." *J. Mar. Sci. Eng.* 2 (1): 1–17. <https://doi.org/10.3390/jmse2010001>.
- Wu, L., C. Chen, P. Guo, M. Shi, J. Qi, and J. Ge. 2011. "A FVCOM-based unstructured grid wave, current, sediment transport model, I. Model description and validation." *J. Ocean Univ. China* 10 (Mar): 1–8. <https://doi.org/10.1007/s11802-011-1788-3>.
- Yossef, M. F. M., and H. J. de Vriend. 2010. "Sediment exchange between a river and its groyne fields: Mobile-bed experiment." *J. Hydraul. Eng.* 136 (9): 610–625. [https://doi.org/10.1061/\(ASCE\)HY.1943-7900.0000226](https://doi.org/10.1061/(ASCE)HY.1943-7900.0000226).
- Yossef, M. F. M., and H. J. de Vriend. 2011. "Flow details near river groynes: Experimental investigation." *J. Hydraul. Eng.* 137 (May): 504–516. [https://doi.org/10.1061/\(ASCE\)HY.1943-7900.0000326](https://doi.org/10.1061/(ASCE)HY.1943-7900.0000326).
- Zhou, Z., J. Ge, D. S. van Maren, Z. B. Wang, Y. Kuai, and P. Ding. 2021. "Study of sediment transport in a tidal channel-shoal system: Lateral effects and slack-water dynamics." *J. Geophys. Res.: Oceans* 126 (3): e2020JC016334. <https://doi.org/10.1029/2020JC016334>.
- Zhou, Z., J. Ge, Z. B. Wang, D. S. Maren, J. Ma, and P. Ding. 2019. "Study of lateral flow in a stratified tidal channel-shoal system: The importance of intratidal salinity variation." *J. Geophys. Res.: Oceans* 124 (9): 6702–6719. <https://doi.org/10.1029/2019JC015307>.